Check for updates

All-perovskite tandem solar cells with 24.2% certified efficiency and area over 1 cm² using surface-anchoring zwitterionic antioxidant

Ke Xiao[1,2,7], Renxing Lin[1,7], Qiaolei Han[1,7], Yi Hou[3], Zhenyuan Qin[4], Hieu T. Nguyen[5], Jin Wen[1], Mingyang Wei[3], Vishal Yeddu[6], Makhsud I. Saidaminov[6], Yuan Gao[1], Xin Luo[1,2], Yurui Wang[1], Han Gao[1], Chunfeng Zhang[4], Jun Xu[2], Jia Zhu[1], Edward H. Sargent[3] and Hairen Tan[1✉]

Monolithic all-perovskite tandem solar cells offer an avenue to increase power conversion efficiency beyond the limits of single-junction cells. It is an important priority to unite efficiency, uniformity and stability, yet this has proven challenging because of high trap density and ready oxidation in narrow-bandgap mixed lead–tin perovskite subcells. Here we report simultaneous enhancements in the efficiency, uniformity and stability of narrow-bandgap subcells using strongly reductive surface-anchoring zwitterionic molecules. The zwitterionic antioxidant inhibits Sn^{2+} oxidation and passivates defects at the grain surfaces in mixed lead–tin perovskite films, enabling an efficiency of 21.7% (certified 20.7%) for single-junction solar cells. We further obtain a certified efficiency of 24.2% in 1-cm²-area all-perovskite tandem cells and in-lab power conversion efficiencies of 25.6% and 21.4% for 0.049 cm² and 12 cm² devices, respectively. The encapsulated tandem devices retain 88% of their initial performance following 500 hours of operation at a device temperature of 54–60 °C under one-sun illumination in ambient conditions.

Single-junction pure lead halide perovskite solar cells (PSCs) have seen rapid increases in power conversion efficiency (PCE), with certified values reaching 25.2% for small-area devices (~0.1 cm²)[1–3]. Monolithic all-perovskite tandem solar cells have the potential to deliver higher PCEs than available using single-junction PSCs while maintaining the benefits of low-cost solution processing[4,5]. With recent advances in mixed lead–tin (Pb–Sn) narrow-bandgap PSCs[6–8], the PCEs of small-area all-perovskite tandem solar cells have increased to an impressive 24.8% (refs. [6,9,10]).

Pure lead PSCs have advanced simultaneously in efficiency, stability and scalability[11–13]. Achieving this union remains an important priority for all-perovskite tandem solar cells, but attaining this goal has been curtailed by progress in mixed Pb–Sn narrow-bandgap subcells[14–16]. The diffusion lengths of mixed Pb–Sn perovskite films have been improved to several micrometres, but their efficiency in solar cells is still at or below ~21% (their theoretical PCE limit is comparable to that of lead PSCs)[6,7].

Approaches to mixed Pb–Sn perovskites must address the issue of Sn^{2+} oxidation, occurring prior to, during and following crystallization of the film, even at low concentrations of oxygen[17,18]. Antioxidant additives, such as SnF_2, SnF_2–pyrazine complex and hydroxybenzene sulfonic acid, have been investigated to reduce defect densities related to Sn^{2+} oxidation in pure Sn and mixed Pb–Sn perovskites[17,19,20]. For example, Sn comproportionation addresses the Sn^{2+} oxidation issue in mixed Pb–Sn perovskite inks prior to the crystallization[6].

A recent study revealed that Sn^{2+} can be oxidized even during crystallization, a result of the effect of solvents used in materials processing[21]. This demands a strategy to deal with Sn^{2+} oxidation even during, and immediately following, crystallization of mixed Pb–Sn perovskite films.

Another challenge in fabricating high-quality tin-containing perovskites originates from their nonuniform nucleation and fast crystallization[18,22]. This leads to high trap densities in mixed Pb–Sn perovskite films, as well as nonuniformity in film quality when grown over a large substrate. Defective grain surfaces are vulnerable to trap generation and Sn^{2+} oxidation, and this works against the stability, efficiency and scaling of mixed Pb–Sn PSCs and all-perovskite tandems[7,23,24].

We posited that the electronic quality and stability of mixed Pb–Sn perovskites could be simultaneously improved if defects at the grain surfaces could instead become passivated during film formation, and if surface-anchored passivating molecules could be strongly reductive in order to suppress Sn^{2+} oxidation. We further reasoned that the film uniformity would be improved in concert if the reductive passivating molecules could regulate the crystallization process.

Here we report simultaneous advancements in the efficiency, uniformity and stability of mixed Pb–Sn narrow-bandgap PSCs using a surface-anchoring zwitterionic antioxidant added into the precursor solution. The zwitterionic antioxidant inhibits Sn^{2+} oxidation, passivates defects at the grain surfaces and improves the uniformity of mixed Pb–Sn perovskite films. This enables a high PCE of 21.7% (certified 20.7%) for narrow-bandgap PSCs and a certified PCE of 24.2% for all-perovskite tandem solar cells with an

[1]National Laboratory of Solid State Microstructures, Collaborative Innovation Center of Advanced Microstructures, Jiangsu Key Laboratory of Artificial Functional Materials, College of Engineering and Applied Sciences, Nanjing University, Nanjing, China. [2]School of Electronics Science and Engineering, Nanjing University, Nanjing, China. [3]Department of Electrical and Computer Engineering, University of Toronto, Toronto, ON, Canada. [4]School of Physics, Nanjing University, Nanjing, China. [5]Research School of Electrical, Energy and Materials Engineering, College of Engineering and Computer Science, The Australian National University, Canberra, NSW, Australia. [6]Department of Chemistry, University of Victoria, Victoria, BC, Canada. [7]These authors contributed equally: Ke Xiao, Renxing Lin, Qiaolei Han. ✉e-mail: hairentan@nju.edu.cn

aperture area over $1\,cm^2$. We further obtained in-lab PCEs of 25.6% and 21.4% for tandem cells with aperture areas of $0.049\,cm^2$ and $12\,cm^2$, respectively. Encapsulated tandem devices retained 88% of their initial performance following 500 h of operation at the maximum power point and a device temperature of 54–60 °C under full one-sun illumination in ambient conditions.

Mixed Pb–Sn perovskite films with formamidine sulfinic acid (FSA) additive

We used $FA_{0.7}MA_{0.3}Pb_{0.5}Sn_{0.5}I_3$ as the narrow-bandgap perovskite composition for tandem solar cells, where MA is methylammonium and FA is formamidinium. The mixed Pb–Sn perovskite films were processed by spin-coating of a stoichiometric solution of FAI, MAI, PbI_2 and SnI_2 (with 10 mol% excess SnF_2 relative to SnI_2) in a mixed solvent of dimethyl formamide (DMF) and dimethyl sulfoxide (DMSO). Tin powder was added to suppress Sn^{4+} formation in the precursor solution[6].

A small amount (0.1–1.0 mol% relative to PbI_2 and SnI_2) of FSA, a strong reducing agent used in the textile industry (though its reducibility might be different when coordinated with Pb or Sn ions)[25,26], was added directly into the precursor solution (Fig. 1a). FSA can exist in three different tautomers, of which the zwitterionic form is the most stable one in both the solid state and in perovskite precursor solution[27]. We chose FSA because it unites functionalities to improve the uniformity, electronic quality and stability of mixed Pb–Sn films. First, FSA can coordinate perovskite precursor constituents (for example, PbI_2/SnI_2 and FAI/MAI) to form complexes via dative bonding in the manner achieved using DMSO (Supplementary Fig. 1a and Fig. 1b). Since FSA is less volatile than DMSO, we reasoned that introduction of FSA in the precursor solution could enable delayed, and more-uniform, crystallization (Supplementary Fig. 1b,c). We further reasoned that the zwitterion tautomer of FSA could provide a means to passivate both electron-donating (for example, FA/MA vacancy) and electron-accepting (for example, halide vacancy, under-coordinated Pb^{2+}/Sn^{2+}) defects on the grain surfaces (Fig. 1a). Finally, we hypothesized that surface-anchored FSA, as a strong reducing agent, could reduce Sn^{4+} (if formed during crystallization) back to Sn^{2+} as well as neutralize oxygen molecules (Fig. 1a).

We investigated the effect of the FSA additive on the crystalline structure and morphology of mixed Pb–Sn perovskite films. We refer to the films and devices processed from precursor solution without and with the FSA additive as the control and FSA samples, respectively. X-ray diffraction patterns of the control and FSA films exhibited a single perovskite phase without PbI_2/SnI_2 or non-perovskite phases in each case, and both classes of film showed similar crystallinity and crystallographic orientation (Fig. 1c). Introducing the FSA additive did not affect the surface morphology; both sets of films were pin-hole free with comparable grain size (Supplementary Fig. 2).

We then investigated the antioxidation effect of FSA in precursor solution and in Pb–Sn perovskite film. We found no colour change in Pb–Sn perovskite precursor solution (tin powder was not added) with FSA additive following exposure to air for five minutes (Supplementary Fig. 3a). By contrast, the precursor solution without FSA and tin powder exhibited fast oxidation after exposure to air, as indicated by the colour change from yellow to red. The absorption spectra of the precursor solutions in different stages further confirmed that the FSA additive can effectively suppress the oxidation of Sn^{2+} (Supplementary Fig. 3b). The shift in absorption onset of the FSA solution in comparison to the control also indicates chemical interaction between FSA and PbI_2/SnI_2, likely via the O-based electron donor and sulfinic group[28,29]. X-ray photoelectron spectroscopy (XPS) of the films showed that the FSA additive was present in the perovskite films (Fig. 1d). This is consistent with the fact that it is neither soluble in the antisolvent, nor volatile. We propose that FSA

molecules anchor on the grain surfaces in the perovskite film, with formamidinium and sulfinic groups playing roles as depicted in Fig. 1a. The interaction between FSA and the perovskite film is indicated by a shift in binding energy of the metal cation and the halide (Supplementary Fig. 4). When FSA molecules are introduced, they retard oxidation of Sn^{2+} in mixed Pb–Sn perovskite films upon exposure to air (Fig. 1e). By contrast, the control film without the protection of FSA exhibited rapid Sn^{2+} oxidization (most likely to initiate at the grain surfaces) when exposed to air.

To investigate whether there was a defect passivation effect from the use of FSA, we first measured the steady-state and time-resolved photoluminescence (PL) of the control and FSA mixed Pb–Sn perovskite films. The PL emission intensity of the FSA film is approximately three times higher than that of the control sample (Fig. 2a), indicating that adding FSA reduces the non-radiative recombination in mixed Pb–Sn perovskite films. We further carried out the time-resolved PL decays of the control and FSA films. The PL decay lifetime of the FSA film (188 ns) is longer than that of the control film (64 ns; Fig. 2b). This indicates that the carrier trapping was substantially suppressed upon the introduction of FSA. The space-charge limited current measurements also suggested a lower trap-state density in Pb–Sn perovskite films with FSA (Supplementary Fig. 5), agreeing with previous reports that zwitterionic molecules passivate both negatively and positively charged traps[30,31].

We further carried out femtosecond-resolved optical-pump terahertz-probe (OPTP) spectroscopy for the perovskite films deposited on quartz substrates (Fig. 2c and Supplementary Fig. 6). We obtained similar charge-carrier mobilities of about $60\,cm^2\,V^{-1}\,s^{-1}$ for the FSA and control samples. Due to the longer carrier lifetime, the diffusion length of the FSA sample is increased, suggesting better charge transport through the FSA film. We also performed femtosecond transient absorption spectroscopy to check whether the introduction of FSA would cause any phase segregation within the perovskite film. The film showed photobleaching peaks that remained consistent without noticeable shift for delay times over 1–7,000 ps (Fig. 2d), indicating a substantially spatially uniform phase (bandgap) in the Pb–Sn perovskite films.

We then proceeded to investigate the effect of the FSA additive on film uniformity. We first performed PL intensity imaging of the control and FSA perovskite films deposited on bare glass substrates (Fig. 2e). Stronger PL emission was observed from the FSA samples compared to the controls, consistent with the steady-state PL spectra as shown in Fig. 2a. The control film showed nonuniform emission over the substrate area while the FSA perovskite film exhibited a more-uniform and brighter PL emission over the substrate area (excluding the substrate edges). The zoomed-in micro-PL mapping images further confirm that the FSA film has stronger emission and a larger area with bright emission (Fig. 2f). We further carried out PL and electroluminescence (EL) intensity imaging measurements of complete control and FSA Pb–Sn solar cells fabricated on $2.5 \times 2.5\,cm^2$ substrates with an active area of $0.9 \times 1.4\,cm^2$ at the centre (Supplementary Figs. 7 and 8). The FSA devices showed more homogeneous PL and EL emission than the control devices over the whole active areas. Furthermore, the EL emission intensity of the FSA solar cells was much stronger than that of the control devices at the same applied voltage of 0.8 V (close to the open-circuit voltage, V_{oc}, of solar cells), consistent with the lower trap density and less non-radiative recombination in FSA perovskite films.

Photovoltaic (PV) performance of mixed Pb–Sn PSCs with FSA

To evaluate solar cell performance, we fabricated narrow-bandgap mixed Pb–Sn PSCs without and with the FSA additive, where the perovskite layer is ~850 nm thick (Supplementary Fig. 9). The PSCs had a device structure of ITO/PEDOT-PSS/perovskite/C_{60}/BCP/Cu,
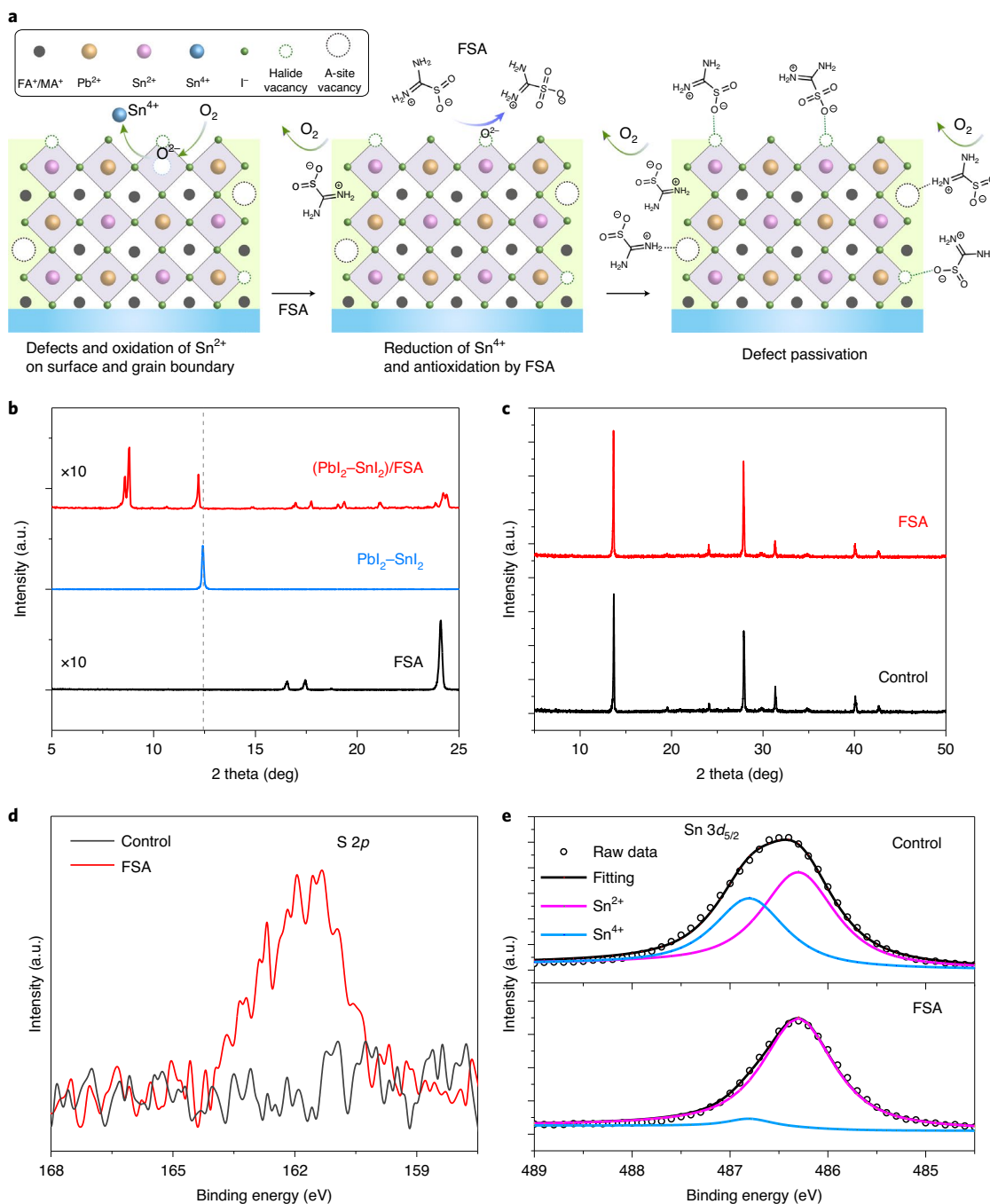
Fig. 1 | Characterization of mixed Pb–Sn narrow-bandgap perovskite films with FSA. a, Schematic illustration of antioxidation and defect passivation at grain surfaces (including film surface and grain boundary) of mixed Pb–Sn perovskite films enabled by FSA. A-site represents the monovalent cation in the perovskites. **b**, X-ray diffraction patterns of FSA, a mixed PbI_2–SnI_2 (1:1 in molar ratio) film and a (PbI_2–SnI_2)/FSA adduct film. The vertical dashed line indicates the diffraction peak position of the mixed PbI_2–SnI_2 film. **c**, X-ray diffraction patterns of the control and FSA perovskite films. **d**, The S $2p$ XPS spectra of the control and FSA perovskite films. **e**, The Sn $3d_{5/2}$ XPS spectra of the control and FSA perovskite films after exposure to air for ~10 min. The original spectra (points) and Gaussian–Lorentzian fitting curves (lines) are shown.

where ITO is indium tin oxide, PEDOT-PSS is poly(3,4-ethylene dioxythiophene)-poly(styrene sulfonate), C_{60} is fullerene and BCP is bathocuproine. For FSA devices, the best PV performance was achieved at the FSA concentration of 0.3 mol% (Supplementary Fig. 10). Unless otherwise stated, this optimal concentration was used for all FSA films and devices discussed in this work. Figure 3a compares the PV parameters of the control and FSA solar cells (aperture area of 0.049 cm²) processed over several identical runs. The FSA

devices exhibited an obvious improvement in average V_{oc} compared to the control ones (0.83 versus 0.80 V; Table 1). The average fill factor (FF) was slightly improved with the FSA additive, while the average short-circuit current density (J_{sc}) remained similar. Correspondingly, the FSA devices had a considerably higher average PCE of 20.4% (19.4% for the control). To find out how passivation affects the charge recombination in solar cells, we conducted transient photovoltage measurements. The charge-recombination lifetime (τ) of the FSA
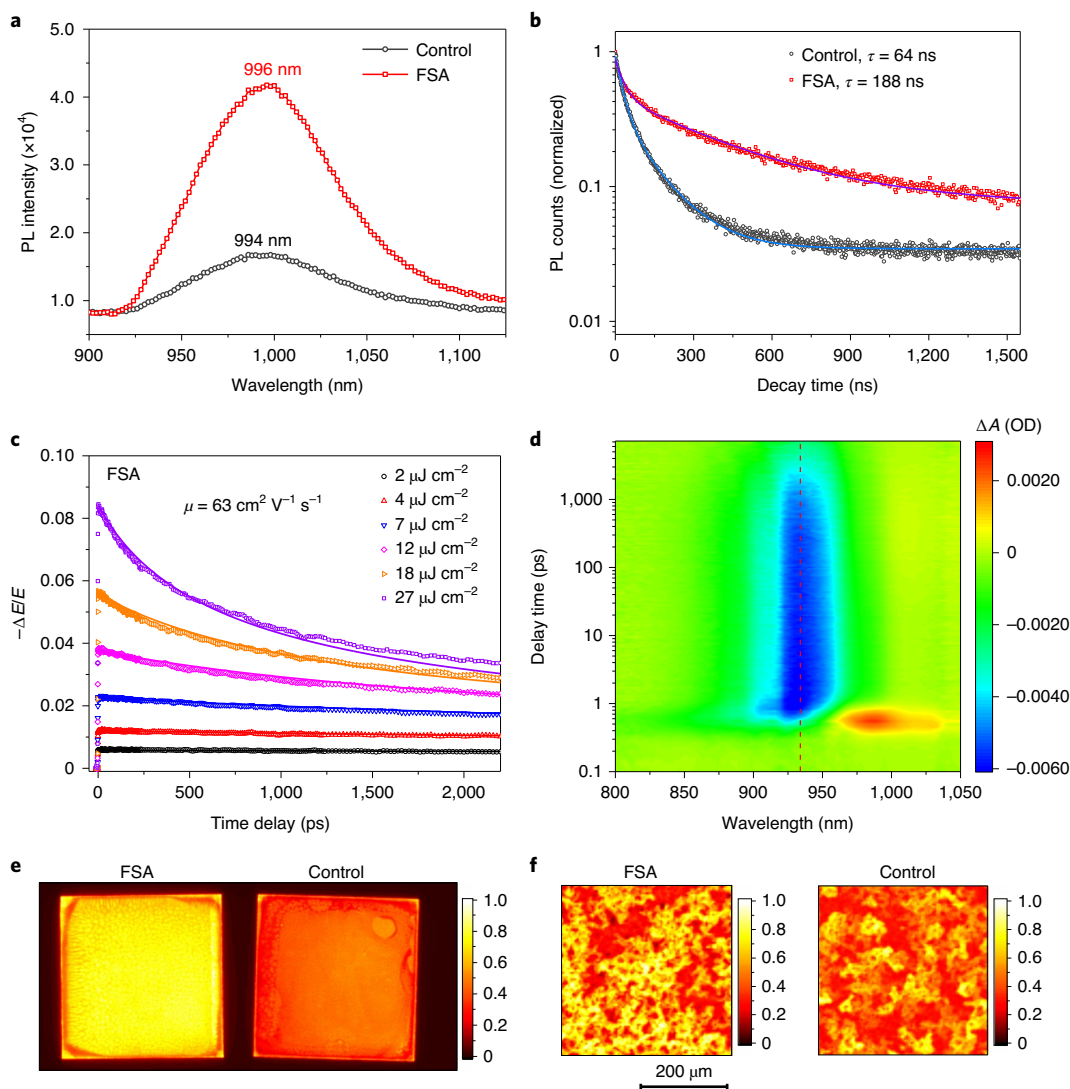
Fig. 2 | Charge dynamics and uniformity of Pb–Sn narrow-bandgap perovskite films with FSA. a,b, Steady-state PL spectra (**a**) and time-resolved PL decays (**b**) of the control and FSA perovskite films deposited on glass substrates. The decay curves were fitted with biexponential components to obtain a fast and a slow decay lifetime. The mean carrier lifetimes τ for the biexponential fit were calculated by the weighted average method. **c**, Femtosecond OPTP transients of the FSA perovskite film measured after excitation with a 90 fs light pulse of 800 nm wavelength with various fluences. The transients were fitted globally according to the equation $dn(t)/dt = -k_3 n^3 - k_2 n^2 - k_1 n$, where t is decay time, and k_1, k_2 and k_3 are rate constants associated with monomolecular recombination, bimolecular recombination and Auger recombination, respectively. The mobility is calculated as 63 $cm^2 V^{-1} s^{-1}$. **d**, Transient absorption study of the FSA film on a glass substrate. The vertical red-dashed line indicates the peak position of the photobleaching band. The colour bar shows the photoinduced absorption change (ΔA). OD, optical density. **e,f**, PL intensity imaging (**e**) and zoomed-in micro-PL mapping (**f**) of the control and FSA films deposited on glass substrates (size of $2.5 \times 2.5 \, cm^2$). The colour bars show the normalized PL intensity. The micro-PL mapping area was $400 \times 400 \, \mu m^2$ with a step size of 5 μm and was selected from the substrate centre.

device was substantially longer than that of the control device (43 versus 10 μs, Supplementary Fig. 11), consistent with lower trap density and reduced carrier trapping in FSA perovskite films.

We fabricated 65 narrow-bandgap FSA solar cells; the histogram of their PCE values is shown in the inset of Fig. 3b. The narrow distribution indicates good reproducibility for Pb–Sn PSCs processed from the precursor solution with FSA additive. The best FSA device achieved a high in-lab PCE of 21.7%, with a V_{oc} of 0.85 V, J_{sc} of 31.6 $mA \, cm^{-2}$ and FF of 80.8% under reverse scan (Fig. 3b). Figure 3c presents the external quantum efficiency (EQE) curve of the champion FSA device, and the integrated J_{sc} value (31.5 $mA \, cm^{-2}$) is in good agreement with the J–V characterization. We sent a FSA narrow-bandgap PSC to the Newport PV test laboratory for independent confirmation, and the device showed a certified PCE

of 20.74% ($V_{oc} = 0.841$ V, $J_{sc} = 30.6 \, mA \, cm^{-2}$ and FF = 80.6%) as shown in Supplementary Fig. 12.

In view of the improved film uniformity with the FSA additive, we further fabricated mixed Pb–Sn PSCs on larger substrates (size of $2.5 \times 2.5 \, cm^2$, device aperture area of 1.05 cm^2). Control devices exhibited a large variation in PV parameters among cells processed in several batches (Supplementary Fig. 13). The devices with FSA additive exhibited a narrower distribution in performance and higher average V_{oc} and J_{sc} values. Correspondingly, FSA devices had a higher average PCE than control devices (17.5% versus 13.9%; Fig. 3e). We observed a large variation in J_{sc} and EQE among eight selected areas (0.049 cm^2) distributed over a control Pb–Sn PSC (Supplementary Fig. 14 and Supplementary Table 1). In contrast to the control device, the FSA device showed much narrower variations
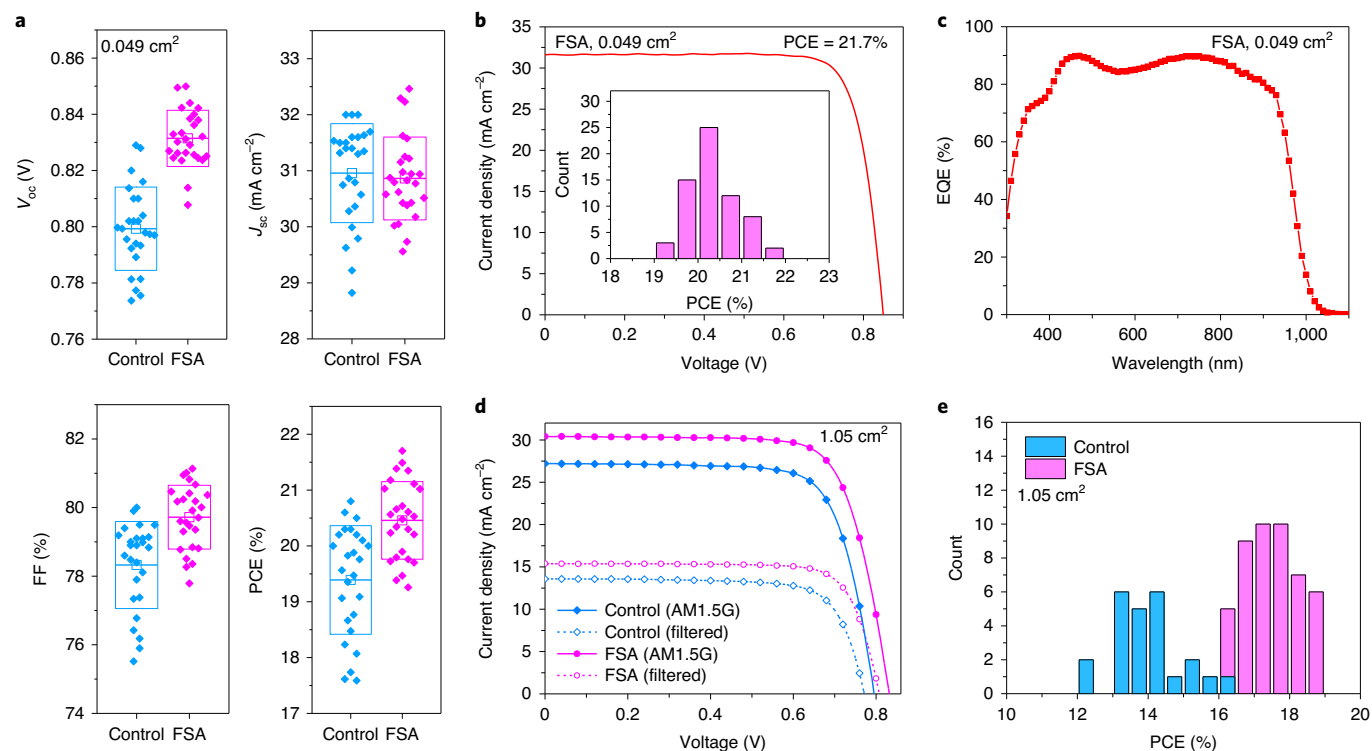
Fig. 3 | PV performance of mixed Pb–Sn narrow-bandgap solar cells. a, Comparison of PV performance between control and FSA narrow-bandgap solar cells (aperture area, 0.049 cm²) processed in the same runs (26 devices for each type). The box lines indicate the standard deviation, and the centre represents the mean value. **b**, The J–V curve of the champion FSA solar cell under a reverse scan. The inset shows the PCE histogram of 65 FSA devices, exhibiting an average PCE of 20.4 ± 0.5%. **c**, The corresponding EQE spectra of the champion FSA device, showing an integrated J_{sc} of 31.5 mA cm⁻². **d**, J–V curves of the champion control and FSA devices (aperture area, 1.05 cm²) measured under AM1.5G and wide-bandgap perovskite filtered illuminations. **e**, Histograms of PCEs for 24 control and 47 FSA solar cells (aperture area, 1.05 cm²), showing average PCEs of 13.9 ± 1.0% and 17.5 ± 0.8%, respectively.

Table 1 | PV performance of the control and FSA mixed Pb–Sn PSCs

Device	Area (cm²)	V_{oc} (V)	J_{sc} (mA cm⁻²)	FF (%)	PCE (%)
Control	0.049	0.829	31.6	79.5	20.8
Average		0.799 ± 0.015	30.9 ± 0.9	78.3 ± 1.2	19.4 ± 1.0
FSA	0.049	0.850	31.6	80.8	21.7
Average		0.832 ± 0.008	30.8 ± 0.7	79.5 ± 1.0	20.4 ± 0.5
Control (AM1.5)	1.05	0.795	27.2	74.4	16.1
Average		0.751 ± 0.027	26.3 ± 1.9	70.7 ± 4.5	13.9 ± 1.0
Filtered		0.771	13.6	74.9	7.8
FSA (AM1.5)	1.05	0.832	30.4	74.4	18.8
Average		0.801 ± 0.016	29.8 ± 0.7	71.7 ± 1.6	17.5 ± 0.8
Filtered		0.808	15.4	77.6	9.7

The devices were measured with an aperture area of 0.049 cm² or 1.05 cm² under full AM1.5G illumination. The 1.05-cm²-area devices were also measured under a filtered spectrum by a wide-bandgap perovskite film to check whether the FF was limited by the conduction of the front electrode.

in J_{sc} and PCE among the eight small-size pixels, agreeing with the better uniformity in electronic quality of the FSA perovskite films. The best-performing FSA device exhibited a PCE of 18.8% under reverse scan (Fig. 3d). The champion control device showed a lower PCE of 16.1%, mainly due to the lower V_{oc} and J_{sc} values (EQE spectra shown in Supplementary Fig. 15).

The FF of single-junction cells with a larger area may be impacted by the insufficient conductivity provided by the front transparent electrodes. We thus carried out J–V measurements of

devices with aperture areas of 1.05 cm² under illumination filtered by a wide-bandgap perovskite film to closely represent the operation in the tandem configuration. The FF of FSA devices increased from 74.4% under full AM1.5G illumination (100 mW cm⁻²) to 77.6% under filtered illumination (Fig. 3d and Table 1). However, the control device exhibited no obvious change in FF under filtered illumination: we propose that its FF value is limited by the inhomogeneity of Pb–Sn perovskite instead of by insufficient conduction within the front electrode.

Performance and stability of all-perovskite tandems

Motivated by the improved uniformity in Pb–Sn perovskite films with FSA, we fabricated monolithic all-perovskite tandem solar cells with a device aperture area of 1.05 cm². The wide-bandgap front subcell had a composition of $Cs_{0.2}FA_{0.8}PbI_{1.8}Br_{1.2}$. The wide-bandgap perovskite films were fabricated from a mixture of six precursors (see details in Methods). We found that wide-bandgap PSCs using six precursors exhibited substantially improved photostability in comparison to the devices made from four precursors (Supplementary Fig. 16), although both perovskite films had notionally the same compositions. The origin of this difference is the subject of further study. The tandem cells had a device structure of glass/ITO/NiO/wide-bandgap perovskite/C_{60}/ALD-SnO$_2$/Au (~1 nm)/PEDOT-PSS/narrow-bandgap perovskite/C_{60}/ALD-SnO$_2$/ Cu, as shown in Fig. 4a,b. The SnO$_2$ layers deposited using atomic layer deposition (ALD-SnO$_2$) at low temperatures were used in the interconnecting layer and as the electron transport layer (ETL) for Pb–Sn subcells.

Here we used solution-processed NiO nanocrystal films as the hole transport layer (HTL) for wide-bandgap perovskite solar cells, where the NiO nanocrystals were synthesized according to previous work[32]. The surface of the NiO films was modified by spin-coating an ultrathin layer (~5 nm) of a thermally cross-linkable p-type small molecule, *N*4,*N*4′-di(naphthalen-1-yl)-*N*4,*N*4′-bis(4-vinylphenyl) biphenyl-4,4′-diamine (VNPB). The cross-linked VNPB has been used as hole-injection material for solution-processed organic light-emitting diodes as well as a hole-extraction layer for PSCs[33,34]. The VNPB modification increased V_{oc} by ~30 mV (Supplementary Fig. 17), likely due to faster hole extraction and reduced interfacial recombination (Supplementary Fig. 18)[35,36]. The good wetting behaviour of perovskite precursor solution on hydrophilic NiO film allows the growth of wide-bandgap perovskite films with better uniformity over the whole substrate area (Supplementary Fig. 19). On average we observed higher PCEs for wide-bandgap cells using NiO than those using a hydrophobic poly(triarylamine)-based (PTAA-based) HTL in 1-cm²-sized devices (Supplementary Fig. 20), although PTAA usually leads to a better performance in small-sized devices (area, ~0.1 cm²). The thicknesses of perovskite layers for the front and back subcells were optimized to be ~350 and 950–1,150 nm, respectively, for FSA tandems, in order to achieve a high matched current density between the subcells (Supplementary Fig. 21).

Figure 4c presents the *J–V* curves of the best-performing FSA and control tandem solar cells measured with an aperture area of 1.05 cm²; the corresponding PV parameters are summarized in Table 2. The champion FSA tandem solar cell exhibited a remarkably high PCE of 24.7% under reverse scan, with a high V_{oc} of 2.012 V, a J_{sc} of 15.5 mA cm⁻² and a high FF of 79.3%. The tandem device had very minor hysteresis between reverse and forward scans (24.7% versus 24.6%). The PCEs from *J–V* sweeps are consistent with the stabilized PCE of 24.6% measured over 6 min (Supplementary Fig. 22). The integrated J_{sc} values of the wide-bandgap and narrow-bandgap subcells from EQE spectra (Fig. 4d) are 16.1 and 15.7 mA cm⁻², respectively, in good agreement with the J_{sc} determined from *J–V* measurements.

We fabricated 40 FSA tandem devices with an aperture area of 1.05 cm² and they provided an average PCE of 23.9%, higher than the average PCE (21.1%) of control devices (Fig. 4e). The narrow PCE distribution indicates an excellent reproducibility of FSA tandem cells. We sent a tandem solar cell (1.05 cm²) to an accredited independent PV calibration and measurement laboratory (Japan Electrical Safety and Environment Technology Laboratories, **JET**) for certification. JET is one of the internationally recognized PV test centres listed in the Solar Cell Efficiency Table[37]. The tandem device delivered a certified stabilized PCE of 24.2% (Supplementary Fig. 23). The certified PCE of 24.2% exceeds those of other thin-film solar cells with areas over 1 cm² (Supplementary Table 2).

In light of the increased performance and uniformity in narrow-bandgap PSCs, we were able to fabricate small-area tandem devices (aperture area of 0.049 cm²) with higher PCEs (champion in-lab PCE of 25.6%) and improved reproducibility (Fig. 4f–h) compared to previous work[6]. A recent work by Albrecht et al. has predicted a detailed balance limit of ~43%, and an empirical limit of 33.6%, for all-perovskite tandem solar cells using the bandgap combination 1.77/1.22 eV (ref. [38]). To reach beyond 30% in PCE, it will be important to overcome today's low J_{sc} and the large V_{oc} deficit (particularly in the wide-bandgap subcell). The low J_{sc} is due to the high primary optical reflection at the front side (Supplementary Fig. 24), parasitic absorption losses in the front transparent electrode and PEDOT-PSS layer, and insufficient light absorption in the narrow-bandgap perovskite absorber. The J_{sc} of the tandem cell can be increased above 17 mA cm⁻² by reducing the optical reflection losses (for example, adding antireflective coating on glass), by using a transparent front electrode with lower near-infrared absorption (for example, hydrogenated indium oxide), by replacing the PEDOT-PSS layer with a more transparent and robust HTL (for example, PTAA[14] and self-assembled monolayer[39]) and by increasing the thickness of the mixed Pb–Sn absorber layer once it also achieves longer carrier diffusion lengths. The V_{oc} of a 1.77-eV-wide-bandgap subcell (~1.2 V in current tandems) is likely to improve above 1.4 V through optimization of the perovskite itself and the device interfaces[36,40]. With the further advances mentioned above, a PCE higher than 30% can be reached if V_{oc} reaches 2.2 V, J_{sc} rises to 17 mA cm⁻² and FF = 82% is achieved, all simultaneously.

We further fabricated several tandem cells with a larger aperture area (12 cm²) on 6×6 cm² substrates to evaluate their upscaling potential. The 12 cm² tandem devices exhibited very minor hysteresis and had the best PCE of 21.4% under a reverse *J–V* scan (Fig. 4i). To up-scale all-perovskite tandem solar cells, scalable coating methods (for example, blade coating) will need to be advanced further both for wide-bandgap and narrow-bandgap perovskites[13]. Charge transport layers and interconnecting layers can be scaled based on thermal evaporation and ALD.

One of the hurdles to long-term stability for all-perovskite tandem solar cells resides in the fact that Sn²⁺ is prone to oxidation and hence to conversion to Sn⁴⁺. We first compared the atmospheric stability of the unencapsulated control and FSA mixed Pb–Sn PSCs under dark storage in dry ambient air (Supplementary Fig. 25). The unencapsulated FSA Pb–Sn PSCs maintained their initial efficiency after storage in air over 15 h. We speculate that FSA molecules anchored at the surface and grain boundaries of the perovskite film helped retard the oxidation of Sn²⁺ and thus maintain the device performance when exposed to air. The V_{oc} and J_{sc} values (and thus PCEs) even slightly increased at the beginning after exposure to air. The increase of V_{oc} and J_{sc} may be related to oxygen-induced defect passivation at the perovskite–ETL interface[41], given that FSA retards the oxidation of Sn²⁺. By contrast, the control devices exhibited a fast degradation immediately when exposed to air and lost >70% of their initial performance after only 8 h.

The unencapsulated FSA tandem solar cells exhibited excellent shelf stability under storage in a nitrogen (N$_2$) glovebox. No obvious degradation in performance was observed after storage for 170 days (Supplementary Fig. 26). We proceeded to investigate the atmospheric stability of tandem solar cells comprising control and FSA Pb–Sn subcells with C_{60}/BCP or C_{60}/ALD-SnO$_2$ as the ETL (Fig. 5a and Supplementary Table 3). We observed comparable PV performance for tandem cells with C_{60}/BCP or C_{60}/ALD-SnO$_2$ as the ETL (Supplementary Fig. 27). The FSA tandem devices showed better atmospheric stability than the control counterparts for both ETL structures. The FSA/ALD-SnO$_2$ tandem cells, with the help of further protection by a robust ALD-SnO$_2$ film, exhibited the best tolerance to oxidation and retained >95% of their initial performance following storage in air over 500 h. This will allow sufficient time
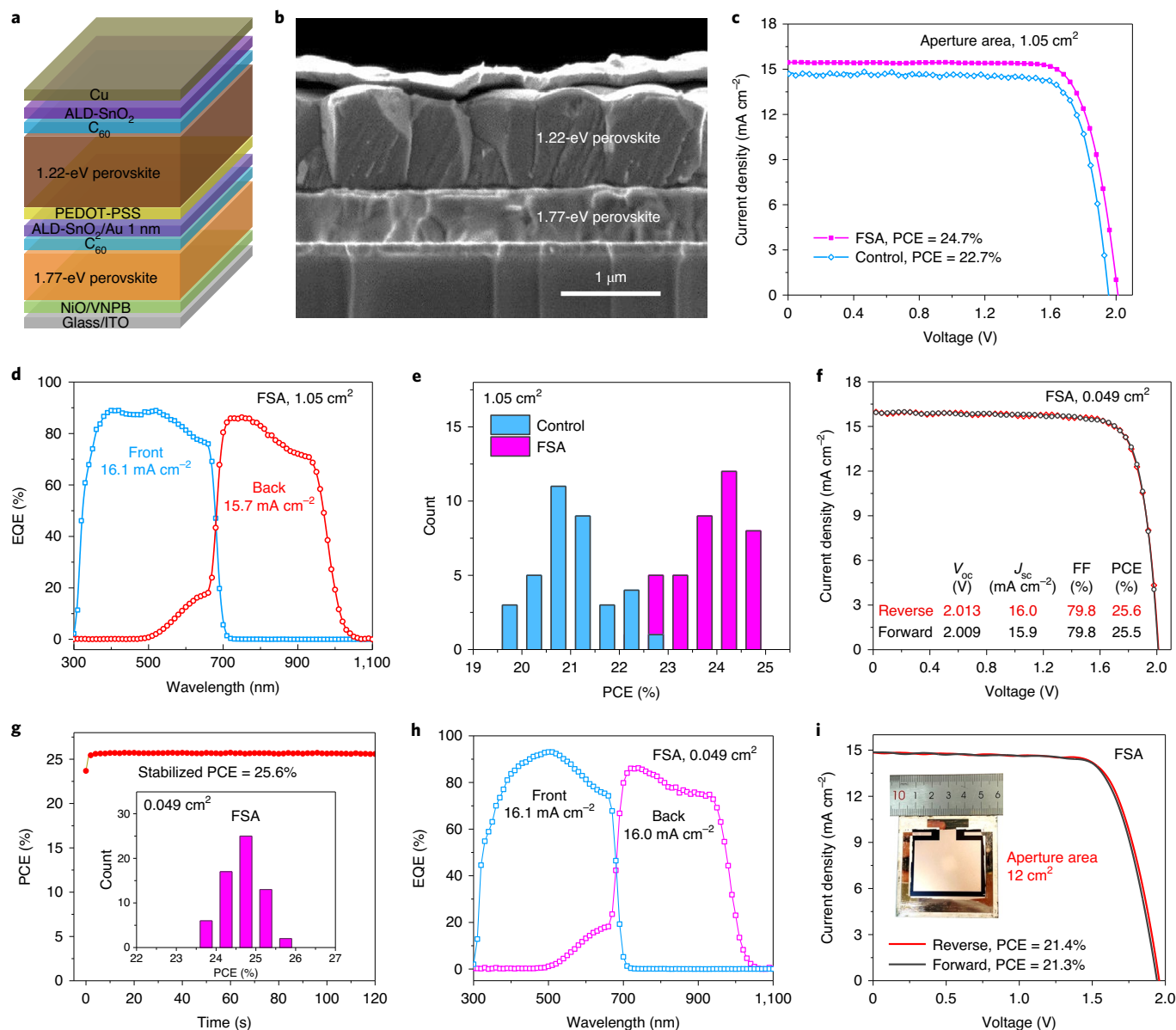
Fig. 4 | PV performance of monolithic all-perovskite tandem solar cells. a,b, Schematic structure (**a**) and cross-sectional scanning electron microscopy image (**b**) of all-perovskite tandem solar cell. **c**, *J–V* curves of the champion control and FSA tandem solar cells (aperture area, 1.05 cm²). **d**, EQE curves of the champion FSA device. The front and back subcells show integrated J_{sc} values of 16.1 and 15.7 mA cm⁻², respectively. **e**, Histogram of PCEs for 36 control and 40 FSA tandem solar cells (1.05 cm²). The devices show average PCEs of 21.1 ± 0.7% and 23.9 ± 0.6%, respectively. **f**, *J–V* curves of the champion FSA tandem cell with an aperture area of 0.049 cm². **g**, Stabilized power output of the champion FSA tandem cell (0.049 cm²). The inset shows the PCE distribution of 63 devices with an average PCE of 24.6 ± 0.4%. **h**, EQE curves of the champion FSA device (0.049 cm²). The front and back subcells show integrated J_{sc} values of 16.1 and 16.0 mA cm⁻², respectively. **i**, *J–V* curves of an FSA tandem cell with an aperture area of 12 cm². The inset shows the digital photo of the corresponding device. The device had a PCE of 21.4% under a reverse scan, with a V_{oc} of 1.958 V, J_{sc} of 14.8 mA cm⁻² and FF of 73.8%.

to complete the encapsulation of modules under ambient conditions before performance degrades obviously, which could reduce the fabrication cost compared to the encapsulation required in an inert environment. To completely prevent long-term degradation due to Sn²⁺ oxidation, further work is still needed to develop oxygen-tolerant narrow-bandgap perovskites, device structures that retard oxygen diffusion into the perovskite layer, and reliable encapsulation that leads to low oxygen permeation.

We then evaluated the operating stability of encapsulated large-area tandem solar cells under constant full one-sun AM1.5 G illumination. We used a Xe-lamp-based solar simulator by continuously tracking the maximum power point (MPP) outputs in ambient

conditions (Fig. 5b). The FSA/ALD-SnO₂ tandem devices retained 88% of their initial performance after over 500 h of MPP tracking. The control/ALD-SnO₂ tandem devices lost more than half of their initial performance following 90 h of operation. We also found that FSA/ALD-SnO₂ tandem devices exhibited better operating stability than the FSA/BCP counterparts, which may be due to the fact that the compact ALD layer could better retard the metal diffusion into the perovskite layers[42,43].

We further carried out stability tests by thermal stressing of devices at 85 °C in a N₂ glovebox without illumination (Supplementary Fig. 28 and Supplementary Table 4). The deployment of ALD-SnO₂ as the ETL improved the thermal stability

Table 2 | PV performance of the champion control and FSA all-perovskite tandem solar cells (aperture area, 1.05 cm²)

Device	Scan direction	V_{oc} (V)	J_{sc} (mA cm⁻²)	FF (%)	PCE (%)
1.77 eV, single	Reverse	1.206	17.1	77.0	15.9
	Forward	1.193	17.1	77.9	15.9
Average	Reverse	1.177 ± 0.009	16.9 ± 0.2	75.2 ± 2.2	15.3 ± 0.2
FSA tandem	Reverse	2.012	15.5	79.3	24.7
	Forward	2.001	15.5	79.3	24.6
Average	Reverse	1.952 ± 0.020	15.1 ± 0.2	80.9 ± 1.1	23.9 ± 0.6
Control tandem	Reverse	1.954	14.7	79.4	22.7
	Forward	1.950	14.7	78.2	22.5
Average	Reverse	1.904 ± 0.020	14.2 ± 0.3	78.0 ± 1.5	21.1 ± 0.7

The average performance (reverse scan) of 25 wide-bandgap PSCs, 40 FSA tandem devices and 36 control tandem devices is provided as well.
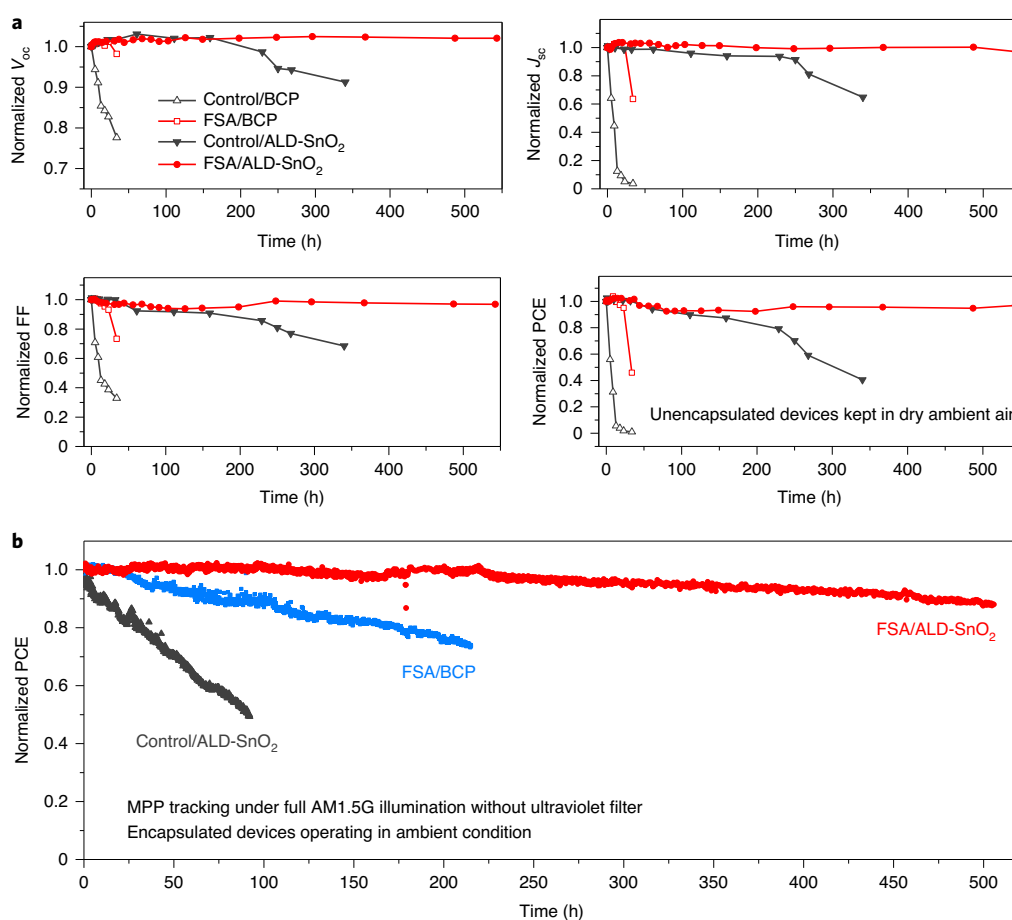

Fig. 5 | Atmospheric and operating stability of all-perovskite tandem solar cells. a, PV performance evolution of unencapsulated tandem solar cells stored under dry ambient air with a humidity of ~20%. Each data point is an average value of four devices. The initial PV parameters are provided in Supplementary Table 3. **b,** Continuous MPP tracking of encapsulated tandem solar cells over 500 h under full simulated AM1.5G illumination (100 mW cm⁻², Xe-lamp simulator) without an ultraviolet filter in ambient air with a humidity of 30–50%. The control/ALD-SnO₂, FSA/BCP and FSA/ALD-SnO₂ devices had initial PCEs of 21.8%, 24.3% and 24.4%, respectively. The device temperature was around 54–60 °C during operation due to the self-heating under solar illumination. There was no passive cooling during device operation, and the environmental temperature was kept at around 25 °C. Control/BCP, control Pb–Sn subcell with C₆₀/BCP as the ETL; control/ALD-SnO₂, control Pb–Sn subcell with C₆₀/ALD-SnO₂ as the ETL; FSA/BCP, FSA Pb–Sn subcell with C₆₀/BCP as the ETL; and FSA/ALD-SnO₂, FSA Pb–Sn subcell with C₆₀/ALD-SnO₂ as the ETL. All devices studied here had aperture areas of 1.05 cm².

of both single-junction and tandem cells. We note that both MA-containing and MA-free narrow-bandgap PSCs exhibited obvious degradation in efficiency, likely due to the reaction between

PEDOT-PSS and mixed Pb–Sn perovskite after thermal stressing[44]. A pressure-tight encapsulation further improved the thermal stability of tandem cells, possibly due to the suppressed outgassing of

volatile products (that is, MA) under thermal stress[45]. The encapsulated FSA/ALD-SnO2 tandem devices maintained 93% of their initial PCE following thermal stress at 85 °C for 228 h. The stability results discussed above indicate the importance of both stable mixed Pb–Sn perovskites and stable device structures to ensure the long-term stability of tandem cells. Replacing the back-metal electrodes with more robust materials such as conductive transparent oxides could give the promise of further improving the long-term stability of all-perovskite tandem solar cells[44].

Conclusions

This work reports surface-anchoring zwitterionic antioxidant additives that enable improved efficiency and stability for monolithic all-perovskite tandem solar cells. The zwitterionic FSA molecules inhibit Sn^{2+} oxidation and passivate defects at the surface and grain boundaries of mixed lead–tin perovskite films, leading to an in-lab PCE of 21.7% (certified 20.7%) in narrow-bandgap solar cells. This advance enabled us to fabricate monolithic all-perovskite tandem solar cells with an in-lab PCE of 24.7% (certified 24.2%) and an area of over 1 cm². The high efficiency united with operational stability in all-perovskite tandem solar cells offers a step towards the viability of this emerging PV technology.

Methods

Materials. All materials were used as received without further purification. The organic halide salts (FAI, FABr, MAI and FAI with purity of >99%) were purchased from GreatCell Solar Materials. PEDOT-PSS aqueous solution (Al 4083) was purchased from Heraeus Clevios. VNPB (>95% purity, lot no. LT-N157) was purchased from Lumtec. PbI_2 (99.999%, lot no. 44314) and SnI_2 (99.999%, lot no. 14476) were purchased from Alfa Aesar. SnF_2 (99%, lot no. 334626), CsI (99.999%, lot no. 203033), CsBr (99.999%, lot no. 203017), DMF (99.8% anhydrous, lot no. 227056), DMSO (99.9% anhydrous, lot no. 276855), FSA (≥98%, lot no. F16001), ethyl acetate (99.8% anhydrous, lot no. 270989) and chlorobenzene (99.8% anhydrous, lot no. 284513) were purchased from Sigma-Aldrich. The C_{60} was purchased from Nano-C. BCP (>99% sublimed) was purchased from Xi'an Polymer Light Technology.

Perovskite precursor solution. For the narrow-bandgap $FA_{0.7}MA_{0.3}Pb_{0.5}Sn_{0.5}I_3$ perovskite, the precursor solution (1.8 M) was prepared in mixed solvents of DMF and DMSO with a volume ratio of 2:1. The molar ratios for FAI/MAI and PbI_2/SnI_2 were 0.7:0.3 and 0.5:0.5, respectively. The molar ratio of $(FAI + MAI)/(PbI_2 + SnI_2)$ was 1:1. SnF_2 (10 mol% relative to SnI_2) was added in the precursor solution. The precursor solution was stirred at room temperature for 2 h. Tin powders (5 mg ml⁻¹) were added in the precursor to reduce Sn^{4+} in the precursor solution. For the FSA solution, formamidine sulfinic acid (0.1–1 mol%) was added to the precursor solution (with tin powders). The precursor solution with the remaining tin powders was filtered through a 0.22 μm polytetrafluoroethylene (PTFE) membrane before making the perovskite films.

Wide-bandgap $FA_{0.8}Cs_{0.2}Pb(I_{0.6}Br_{0.4})_3$ perovskite: unless otherwise stated, the precursor solution (1.1 or 1.2 M) was prepared from six precursors dissolved in mixed solvents of DMF and DMSO with a volume ratio of 4:1. The molar ratios for FAI/FABr/CsI/CsBr and $PbI_2/PbBr_2$ were 0.48:0.32:0.12:0.08 and 0.6:0.4, respectively. The molar ratio of $(FAI + FABr+CsI+CsBr)/(PbI_2 + PbBr_2)$ was 1:1. The precursor solution was stirred at 50 °C for 2 h and then filtered through 0.22 μm PTFE membrane before use. For precursor solution prepared from four precursors (CsI, FAI, PbI_2, and $PbBr_2$), the molar ratio of FAI/CsI/ $PbI_2/PbBr_2$ was 0.8:0.2:0.4:0.6.

Mixed Pb–Sn narrow-bandgap perovskite solar cell fabrication. The pre-patterned ITO glass substrates were sequentially cleaned using acetone and isopropanol. PEDOT-PSS was spin-coated on ITO substrates at 4,000 r.p.m. for 30 s and annealed on a hotplate at 150 °C for 10 min in ambient air. After cooling, we transferred the substrates (1.5 × 1.5 cm² for 0.049-cm²-area devices, 2.5 × 2.5 cm² for 1.05-cm²-area devices) immediately to a nitrogen-filled glovebox for the deposition of perovskite films. The perovskite films were deposited with two-step spin-coating procedures: (1) 1,000 r.p.m. for 10 s with an acceleration of 200 r.p.m. s⁻¹ and (2) 4,000 r.p.m. for 40 s with a ramp-up of 1,000 r.p.m. s⁻¹. Ethyl acetate (150 μl for small-sized devices, 300 μl for 1.05-cm²-sized devices and 600 μl for 12-cm²-sized devices) was dropped on the spinning substrate during the second spin-coating step at 20 s before the end of the procedure. The substrates were then transferred onto a hotplate and heated at 100 °C for 10 min. After cooling to room temperature, the substrates were transferred to the evaporation system. Finally, C_{60} (20 nm), BCP (7 nm) and Cu (100 nm) were sequentially deposited on top of the perovskite by thermal evaporation (Beijing Technol Science Co., Ltd).

Monolithic all-perovskite tandem solar cell fabrication. NiO nanocrystals were synthesized according to previous reports[32]. NiO nanocrystal (25 mg ml⁻¹ in water) layers were first spin-coated on ITO substrates at 3,000 r.p.m. for 30 s and annealed on a hotplate at 130 °C for 30 min in air. After cooling, the substrates were immediately transferred to the glovebox. VNPB (0.5 mg ml⁻¹) in chlorobenzene without doping was spin-coated on the NiO film at 6,000 r.p.m. for 30 s and was then annealed at 150 °C for 10 min. The wide-bandgap perovskite films (1.1 M for control devices, 1.2 M for FSA devices) were deposited on top of VNPB-modified NiO with a two-step spin-coating procedure. The first step was 2,000 r.p.m. for 10 s with an acceleration of 200 r.p.m. s⁻¹. The second step was 6,000 rpm for 40 s with a ramp-up of 2,000 r.p.m. s⁻¹. Chlorobenzene (200 μl for 1.05-cm²-sized devices, 500 μl for 12-cm²-sized devices) was dropped on the spinning substrate during the second spin-coating step at 20 s before the end of the procedure. The substrates were then transferred onto a hotplate and heated at 100 °C for 15 min. After cooling to room temperature, the substrates were transferred to the evaporation system, and a 20-nm-thick C_{60} film was subsequently deposited on top by thermal evaporation at a rate of 0.2 Å s⁻¹. The substrates were then transferred to the ALD system (Veeco Savannah S200) to deposit 20 nm SnO2 at low temperatures (typically 100 °C) using precursors of tetrakis(dimethylamino) tin(IV) (99.9999%, Nanjing Ai Mou Yuan Scientific Equipment) and deionized water. After ALD deposition, the substrates were transferred back to the thermal evaporation system to deposit an ultrathin layer of Au clusters (~1 nm) on ALD-SnO2. PEDOT-PSS layers were spin-cast on top of SnO2-protected front cells and annealed in air at 120 °C for 20 min. After the substrates had cooled, we immediately transferred the substrates to a nitrogen-filled glovebox for the deposition of narrow-bandgap perovskite films with procedures identical to those used for the single-junction devices. The Pb–Sn precursor solution concentration was increased to 2.0–2.2 M to obtain a thickness of ~950–1,150 nm. Finally, 20 nm C_{60}, 7 nm BCP and 100 nm Cu films were sequentially deposited by thermal evaporation at the rates of 0.2, 0.2 and 1.0 Å s⁻¹, respectively. For Pb–Sn subcells with ALD-SnO2 as the ETL, the BCP layer was replaced by an ALD-SnO2 layer (~15 nm), which was deposited at low temperatures (typically 70 °C) to avoid any damage to the Pb–Sn perovskite absorber layer. Details on the deposition conditions of ALD-SnO2 layers can be found in Supplementary Table 5.

Characterization of solar cells. For single-junction solar cells, the J–V characteristics were measured using a Keithley 2400 sourcemeter under the illumination of the solar simulator (EnliTech, Class AAA) at a light intensity of 100 mW cm⁻² as checked with a calibrated reference solar cell (NREL) with a quartz window (a KG-5 reference cell was used for the measurements of wide-bandgap solar cell). Unless otherwise stated, the J–V curves were all measured in a nitrogen-filled glovebox with a scanning rate of 100 mV s⁻¹ (voltage steps of 10 mV and a delay time of 100 ms). The active area was determined by the aperture shade masks (0.049, 1.05 or 12 cm²) placed in front of the solar cells. EQE measurements were performed in ambient air using a QE system (EnliTech) with monochromatic light focused on a device pixel and a chopper frequency of 20 Hz. For tandem solar cells, the J–V characteristics were carried out according to previous work[6]. The spectrum from the simulator was finely tuned to ensure that spectral mismatch was within 3% for both subcells. The solar simulator was set at the light intensity of 100 mW cm⁻² as checked with a calibrated crystalline silicon reference solar cell with a quartz window. EQE measurements were performed in ambient air, and the bias illumination from highly bright LEDs with emission peaks of 850 and 460 nm was used for the measurements of the front subcells and back subcells, respectively.

Stability tests of solar cells. The operational stability tests were carried out under full AM1.5G illumination (Xenon lamp solar simulator, 100 mW cm⁻²) using a home-build LabVIEW-based MPP tracking system using a 'perturb and observe' method in ambient conditions with humidity of 30–50%. The solar cells were encapsulated with a cover glass and ultraviolet epoxy (Three Bond), which was cured under an ultraviolet light-emitting diode lamp (peak emission at 365 nm) for 3 min. Encapsulation details are in Supplementary Fig. 29. No ultraviolet filter was applied during operation. The environmental temperature was kept at around 25 °C (varied between 21–26 °C). The solar cell temperature increased to 54–60 °C under illumination as no passive cooling was implemented to the measurement stage. The illumination intensity was regularly calibrated to compensate for the degradation of the xenon lamp. The dark long-term shelf stability assessments of solar cells (without encapsulation) were carried out by repeating the J–V characterizations over various times, and the devices were stored in a N_2 glovebox. The atmospheric stability tests of solar cells (without encapsulation) were carried out by repeating the J–V characterizations over various times. The devices were stored in a dry-air box with humidity below 20%.

Steady-state and time-resolved PL. Steady-state PL and time-resolved PL were measured using a Horiba Fluorolog time-correlated single-photon-counting system with photomultiplier tube detectors. The light was illuminated from the top surface of the perovskite film. For steady-state PL measurements, the excitation source was from a monochromated Xe lamp (peak wavelength at 520 nm with a line width of 2 nm). For time-resolved PL, a green laser diode (wavelength, $\lambda = 540$ nm) was used for the excitation source with an excitation power density of 5 mW cm⁻². The PL

decay curves were fitted with biexponential components to obtain a fast and a slow decay lifetime. The mean carrier lifetimes τ for the biexponential fit were calculated by the weighted average method (Supplementary Table 6).

Two-dimensional PL and EL imaging. The PL imaging tool is an LIS-R1 system sourced from BT Imaging. The samples were excited with a continuous-wave 808 nm laser (one-sun on-sample intensity). The system had a built-in 950 nm longpass filter to reject the laser light. The camera was a 1,024 × 1,024 pixel, charge-coupled-device silicon detector with a detection range of 400–1,060 nm. The pixel resolution was ~162 μm. The EL imaging tool is a custom-built system. The solar cells were biased with a supplied voltage of 0.8 V and the current was monitored with a Metrohm Autolab PGSTAT128N potentiostat. Measurements were taken once the current reached a steady state. Images were captured using a Princeton Instruments Pixis 1024 camera silicon detector whose detection range was between 400–1,060 nm. The pixel resolution was ~14.6 μm.

Micro-PL mapping. The micro-PL mapping tool was a Horiba LabRAM system equipped with confocal optics, an InGaAs detector (detection range of 800–1,650 nm) and an automatic $X–Y$ mapping stage. The excitation source was a continuous-wave 532 nm laser. The excitation light was focused onto the sample surface using a ×10 objective lens (numerical aperture of 0.25). The on-sample diameter and power of the illumination spot were ~2.6 μm and ~20 μW, respectively. The scanning step size was 5 μm in both the X and Y directions.

Femtosecond OPTP spectroscopy. A commercial Ti–sapphire amplified laser (Libra, Coherent) with a pulse duration of 90 fs, centre wavelength of 800 nm and repetition rate of 1 kHz was used to generate terahertz radiation via optical rectification in a 0.5-mm-thick ZnTe(110) nonlinear single crystal and detect it using free space electro-optic sampling in a 0.5-mm-thick ZnTe(110) crystal. Perovskite thin films deposited on z-cut quartz substrates were photoexcited at 800 nm with fluences ranging from 1.5–50 μJ cm^{-2}. The change in terahertz amplitude was monitored as a function of the time delay between the 800 nm optical-pump pulse and terahertz-probe pulse using a translation stage. All measurements were carried out in a nitrogen-purged environment to avoid potential degradation of perovskite films in ambient air. As the excitation fluence increased, the OPTP transients exhibited accelerated decay dynamics at higher initial photoinjected charge-carrier densities due to enhanced contributions from bimolecular recombination and Auger recombination. We extracted the rate constants associated with different recombination mechanisms by global fits to these transients according to the following rate equation[46]:

$$\frac{\mathrm{d}n(t)}{\mathrm{d}t} = -k_3 n^3 - k_2 n^2 - k_1 n$$

We find the charge-carrier diffusion length L_D (using carrier lifetime τ obtained from PL decays) with the aid of the equation, $L_D = (\mu k_B T/(qR))^{1/2}$ as a function of the charge-carrier density n, where μ is the charge-carrier mobility, $R = k_1 + nk_2 + n^2 k_3$ is the total recombination rate, k_1 is $1/\tau$, k_B is the Boltzmann constant, T is temperature and q is the elementary charge. A carrier density of 10^{15} cm^{-3} (one-sun condition) was used as representative of typical operating conditions for a solar cell.

Femtosecond transient absorption measurements. Femtosecond laser pulses were produced using a regeneratively amplified Yb-KGW laser at a 5 kHz repetition rate (Light Conversion, Pharos). The pump pulse was generated by passing a portion of the 1,030 nm probe pulse through an optical parametric amplifier (Light Conversion, Orpheus) with the second harmonic of the signal pulse selected for 400 nm light. Both the pump and probe pulses (pulse duration 250 fs) were directed into an optical bench (Ultrafast, Helios), where a white-light continuum was generated by focusing the 1,030 nm probe pulse through a sapphire crystal. The time delay was adjusted by optically delaying the probe pulse, with time steps increasing exponentially. A chopper was used to block every other pump pulse and each probe pulse was measured by a charge-coupled device after dispersion by a grating spectrograph (Ultrafast, Helios). Samples were prepared on a glass substrate and translated at 1 mm s^{-1} during the measurement. Pump fluences were kept at 4 μJ cm^{-2}.

Space-charge limited current. The hole-only and electron-only devices were fabricated to obtain the density of hole traps or electron traps using the following architectures: ITO/PEDOT-PSS/perovskite/PTAA/Au for holes, where the PTAA layer was doped with 5 wt% 4-isopropyl-4'-methyldiphenyliodoniumtetrakis (pentafluorophenyl)borate (TPFB), and ITO/TiO$_2$-Cl/PCBM/perovskite/C$_{60}$/BCP/Cu for electrons, where PCBM is [6,6]-phenyl C61 butyric acid methyl ester. Measurements were carried out in a glovebox using a Keithley 2400 sourcemeter. The trap density N_{trap} is determined by the equation, $V_{TFL} = qN_{trap}L^2/(2\varepsilon\varepsilon_0)$, where V_{TFL} is the trap-filled limit voltage, L is the thickness of the perovskite film, ε is the relative dielectric constant of perovskite and ε_0 is the vacuum permittivity.

Optical simulation of tandem solar cells. To further optimize the optical performance of the tandem cell, we used a validated optical model GenPro4 as

developed by Delft University of Technology to minimize the current mismatch between two subcells. The complex refractive index of each layer was measured by a spectroscopic ellipsometer (J.A. Woollam). The implied photocurrent density of each subcell can be calculated with GenPro4 by assuming that the individual absorptances of the top and bottom cells are equivalent to the EQE values of the two cells, respectively. We also assumed that the current density of the tandem cell is determined by the lower current density between the two subcells.

Other characterizations. Scanning electron microscopy images were obtained using a TESCAN microscope with an accelerating voltage of 2 kV. X-ray diffraction patterns were collected using a Rigaku MiniFlex 600 diffractometer equipped with a NaI scintillation counter and using monochromatized Cu–Kα radiation ($\lambda = 1.5406$ Å). XPS analysis was carried out using the Thermo Scientific Al K-Alpha XPS system with energy steps of 0.1 eV. Optical absorption measurements were carried out in a Lambda 950 ultraviolet–visible spectrophotometer. Transient photovoltage decays were measured on a homemade system. A 540 nm green light-emitting diode was used to modulate the V_{oc} with a constant light bias, and the repetition rate was set to 2,000 Hz. A white light-emitting diode was illuminated on the active area of the solar cell under study for the constant light bias. The intensity of the pulsed illumination was set in a way that the modulated V_{oc} was ~10 mV to ensure a perturbation regime. The open-circuit voltage transient, induced by the light perturbation, was measured with a digital oscilloscope set to an input impedance of 1 MΩ. The charge recombination lifetime was fitted by a single exponential decay.

Data availability
All data generated or analysed during this study are included in the published article and its Supplementary Information and Source Data files. Source data are provided with this paper.

References
1. Min, H. et al. Efficient, stable solar cells by using inherent bandgap of α-phase formamidinium lead iodide. *Science* **366**, 749–753 (2019).
2. Jiang, Q. et al. Surface passivation of perovskite film for efficient solar cells. *Nat. Photon.* **13**, 460–466 (2019).
3. Green, M. A. et al. Solar cell efficiency tables (version 55). *Prog. Photovoltaics Res. Appl.* **28**, 3–15 (2020).
4. Eperon, G. E., Hörantner, M. T. & Snaith, H. J. Metal halide perovskite tandem and multiple-junction photovoltaics. *Nat. Rev. Chem.* **1**, 0095 (2017).
5. Leijtens, T., Bush, K. A., Prasanna, R. & McGehee, M. D. Opportunities and challenges for tandem solar cells using metal halide perovskite semiconductors. *Nat. Energy* **3**, 828–838 (2018).
6. Lin, R. et al. Monolithic all-perovskite tandem solar cells with 24.8% efficiency exploiting comproportionation to suppress Sn(ii) oxidation in precursor ink. *Nat. Energy* **4**, 864–873 (2019).
7. Tong, J. et al. Carrier lifetimes of >1 μs in Sn-Pb perovskites enable efficient all-perovskite tandem solar cells. *Science* **364**, 475–479 (2019).
8. Zhao, D. et al. Efficient two-terminal all-perovskite tandem solar cells enabled by high-quality low-bandgap absorber layers. *Nat. Energy* **3**, 1093–1100 (2018).
9. Eperon, G. E. et al. Perovskite-perovskite tandem photovoltaics with optimized band gaps. *Science* **354**, 861–865 (2016).
10. Palmstrom, A. F. et al. Enabling flexible all-perovskite tandem solar cells. *Joule* **3**, 2193–2204 (2019).
11. Rong, Y. et al. Challenges for commercializing perovskite solar cells. *Science* **361**, eaat8235 (2018).
12. Park, N., Grätzel, M., Miyasaka, T., Zhu, K. & Emery, K. Towards stable and commercially available perovskite solar cells. *Nat. Energy* **1**, 16152 (2016).
13. Park, N.-G. & Zhu, K. Scalable fabrication and coating methods for perovskite solar cells and solar modules. *Nat. Rev. Mater.* **5**, 333–350 (2020).
14. Werner, J. et al. Improving low-bandgap tin–lead perovskite solar cells via contact engineering and gas quench processing. *ACS Energy Lett.* **5**, 1215–1223 (2020).
15. Zeng, L. et al. 2D-3D heterostructure enables scalable coating of efficient low-bandgap Sn–Pb mixed perovskite solar cells. *Nano Energy* **66**, 104099 (2019).
16. Gu, S. et al. Tin and mixed lead–tin halide perovskite solar cells: progress and their application in tandem solar cells. *Adv. Mater.* **32**, 1907392 (2020).
17. Ma, L. et al. Carrier diffusion lengths of over 500 nm in lead-free perovskite CH$_3$NH$_3$SnI$_3$ films. *J. Am. Chem. Soc.* **138**, 14750–14755 (2016).
18. Konstantakou, M. & Stergiopoulos, T. A critical review on tin halide perovskite solar cells. *J. Mater. Chem. A* **5**, 11518–11549 (2017).

19. Lee, S. J. et al. Fabrication of efficient formamidinium tin iodide perovskite solar cells through SnF$_2$–pyrazine complex. *J. Am. Chem. Soc.* **138**, 3974–3977 (2016).

20. Tai, Q. et al. Antioxidant grain passivation for air-stable tin-based perovskite solar cells. *Angew. Chem. Int. Ed.* **58**, 806–810 (2019).

21. Saidaminov, M. I. et al. Conventional solvent oxidizes Sn(II) in perovskite inks. *ACS Energy Lett.* **5**, 1153–1155 (2020).

22. Ke, W., Stoumpos, C. C. & Kanatzidis, M. G. "Unleaded" perovskites: status quo and future prospects of tin-based perovskite solar cells. *Adv. Mater.* **31**, 1803230 (2019).

23. Wei, M. et al. Combining efficiency and stability in mixed tin–lead perovskite solar cells by capping grains with an ultrathin 2D layer. *Adv. Mater.* **32**, 1907058 (2020).

24. Ni, Z. et al. Resolving spatial and energetic distributions of trap states in metal halide perovskite solar cells. *Science* **367**, 1352–1358 (2020).

25. Czajkowski, W. & Misztal, J. The use of thiourea dioxide as reducing agent in the application of sulphur dyes. *Dye. Pigment.* **26**, 77–81 (1994).

26. Krug, P. Thiourea dioxide (formamidinesulphinic acid) a new reducing agent for textile printing. *J. Soc. Dye. Colour.* **69**, 606–611 (2008).

27. Lewis, D., Mama, J. & Hawkes, J. An investigation into the structure and chemical properties of formamidine sulfinic acid. *Appl. Spectrosc.* **68**, 1327–1332 (2014).

28. Liu, C., Cheng, Y. & Ge, Z. Understanding of perovskite crystal growth and film formation in scalable deposition processes. *Chem. Soc. Rev.* **49**, 8–12 (2020).

29. Zheng, X. et al. Dual functions of crystallization control and defect passivation enabled by sulfonic zwitterions for stable and efficient perovskite solar cells. *Adv. Mater.* **30**, 1803428 (2018).

30. Wang, Z. et al. Passivation of grain boundary by squaraine zwitterions for defect passivation and efficient perovskite solar cells. *ACS Appl. Mater. Interfaces* **11**, 10012–10020 (2019).

31. Chen, B., Rudd, P. N., Yang, S., Yuan, Y. & Huang, J. Imperfections and their passivation in halide perovskite solar cells. *Chem. Soc. Rev.* **48**, 3842–3867 (2019).

32. Han, Q. et al. Low-temperature processed inorganic hole transport layer for efficient and stable mixed Pb–Sn low-bandgap perovskite solar cells. *Sci. Bull.* **64**, 1399–1401 (2019).

33. Xu, J. et al. Crosslinked remote-doped hole-extracting contacts enhance stability under accelerated lifetime testing in perovskite solar cells. *Adv. Mater.* **28**, 2807–2815 (2016).

34. Hayashi, N., Nishio, R. & Takada, S. Composition, film using the composition, charge transport layer, organic electroluminescence device, and method for forming charge transport layer. US patent US20120080666A1 (2012).

35. Jošt, M. et al. 21.6%-efficient monolithic perovskite/Cu(In,Ga)Se$_2$ tandem solar cells with thin conformal hole transport layers for integration on rough bottom cell surfaces. *ACS Energy Lett.* **4**, 583–590 (2019).

36. Xu, J. et al. Triple-halide wide–band gap perovskites with suppressed phase segregation for efficient tandems. *Science* **367**, 1097–1104 (2020).

37. Green, M. A. et al. Solar cell efficiency tables (version 51). *Prog. Photovoltaics Res. Appl.* **26**, 3–12 (2018).

38. Jošt, M., Kegelmann, L., Korte, L. & Albrecht, S. Monolithic perovskite tandem solar cells: a review of the present status and advanced characterization methods toward 30% efficiency. *Adv. Energy Mater.* **10**, 1904102 (2020).

39. Al-Ashouri, A. et al. Conformal monolayer contacts with lossless interfaces for perovskite single junction and monolithic tandem solar cells. *Energy Environ. Sci.* **12**, 3356–3369 (2019).

40. Gharibzadeh, S. et al. Record open-circuit voltage wide-bandgap perovskite solar cells utilizing 2D/3D perovskite heterostructure. *Adv. Energy Mater.* **9**, 1803699 (2019).

41. Godding, J. S. W. et al. Oxidative passivation of metal halide perovskites. *Joule* **3**, 2716–2731 (2019).

42. Raiford, J. A. et al. Enhanced nucleation of atomic layer deposited contacts improves operational stability of perovskite solar cells in air. *Adv. Energy Mater.* **9**, 1902353 (2019).

43. Seo, S., Jeong, S., Bae, C., Park, N.-G. & Shin, H. Perovskite solar cells with inorganic electron- and hole-transport layers exhibiting long-term (≈500 h) stability at 85 °C under continuous 1 sun illumination in ambient air. *Adv. Mater.* **30**, 1801010 (2018).

44. Prasanna, R. et al. Design of low bandgap tin–lead halide perovskite solar cells to achieve thermal, atmospheric and operational stability. *Nat. Energy* **4**, 939–947 (2019).

45. Shi, L. et al. Gas chromatography–mass spectrometry analyses of encapsulated stable perovskite solar cells. *Science* **368**, eaba2412 (2020).

46. Wehrenfennig, C., Eperon, G. E., Johnston, M. B., Snaith, H. J. & Herz, L. M. High charge carrier mobilities and lifetimes in organolead trihalide perovskites. *Adv. Mater.* **26**, 1584–1589 (2014).

Acknowledgements

Author contributions

H.T. conceived and directed the overall project. K.X., R.L. and Q.H. fabricated all the devices and conducted the characterization. Y.H., M.I.S., V.Y., X.L., Z.Q., Y.W., J.W., H.G., C.Z., J.X. and J.Z. helped with the device fabrication and material characterization. M.W. performed the steady-state/transient PL and transient absorption measurements. H.T.N. performed the EL and PL imaging characterization. Y.G. performed the optical modelling of tandem devices. H.T. and K.X. wrote the draft, and E.H.S., M.I.S. and Y.H. improved the manuscript. All authors read and commented on the manuscript.

Competing interests

The authors declare no competing interests.

Additional information

nature research

Corresponding author(s):   Hairen Tan

Solar Cells Reporting Summary

Nature Research wishes to improve the reproducibility of the work that we publish. This form is intended for publication with all accepted papers reporting the characterization of photovoltaic devices and provides structure for consistency and transparency in reporting. Some list items might not apply to an individual manuscript, but all fields must be completed for clarity.

For further information on Nature Research policies, including our data availability policy, see Authors & Referees.

▶ Experimental design

Please check: are the following details reported in the manuscript?

1. **Dimensions**

   Area of the tested solar cells
   ☒ Yes ☐ No
   Aperture areas of 0.049 and 1.05 cm2 were used in this work.

   Method used to determine the device area
   ☒ Yes ☐ No
   Black metal aperture masks were used during the J-V measurements.

2. **Current-voltage characterization**

   Current density-voltage (J-V) plots in both forward and backward direction
   ☒ Yes ☐ No
   Provided in this manuscript.

   Voltage scan conditions
   For instance: scan direction, speed, dwell times
   ☒ Yes ☐ No
   Provided in Method section.

   Test environment
   For instance: characterization temperature, in air or in glove box
   ☒ Yes ☐ No
   Provided in Method section.

   Protocol for preconditioning of the device before its characterization
   ☐ Yes ☒ No
   No preconditioning was used in this work.

   Stability of the J-V characteristic
   Verified with time evolution of the maximum power point or with the photocurrent at maximum power point; see ref. 7 for details.
   ☒ Yes ☐ No
   Stabilized PCEs of both single-junction and tandem solar cells were provided.

3. **Hysteresis or any other unusual behaviour**

   Description of the unusual behaviour observed during the characterization
   ☒ Yes ☐ No
   Very minor hysteresis was observed for devices herein.

   Related experimental data
   ☒ Yes ☐ No
   J-V curves under reverse and forward scans were provided.

4. **Efficiency**

   External quantum efficiency (EQE) or incident photons to current efficiency (IPCE)
   ☒ Yes ☐ No
   EQE curves were provided.

   A comparison between the integrated response under the standard reference spectrum and the response measure under the simulator
   ☒ Yes ☐ No
   The integrated Jsc values from QE were consistent with Jsc values from J-V measurements.

   For tandem solar cells, the bias illumination and bias voltage used for each subcell
   ☒ Yes ☐ No
   Stated in Method section.

5. **Calibration**

   Light source and reference cell or sensor used for the characterization
   ☒ Yes ☐ No
   Stated in Method section.

   Confirmation that the reference cell was calibrated and certified
   ☒ Yes ☐ No
   The reference cells were calibrated by NREL and explained in Method.

Calculation of spectral mismatch between the reference cell and the devices under test

☐ Yes
☒ No

The light spectrum used for measurements matches well with the reference silicon cell, and we did not calculate the spectral mismatch between the reference cell and the tested devices

6. Mask/aperture

Size of the mask/aperture used during testing

☒ Yes
☐ No

Metal aperture masks with areas of 0.049 and 1.05 cm2 were used for testing.

Variation of the measured short-circuit current density with the mask/aperture area

☐ Yes
☒ No

We measured all devices with masks.

7. Performance certification

Identity of the independent certification laboratory that confirmed the photovoltaic performance

☒ Yes
☐ No

Pb-Sn PSC was certified by Newport; tandem PSC was certified by JET.

A copy of any certificate(s)
Provide in Supplementary Information

☒ Yes
☐ No

Provided in the supplementary information.

8. Statistics

Number of solar cells tested

☒ Yes
☐ No

Stated in the manuscript.

Statistical analysis of the device performance

☒ Yes
☐ No

Stated in the manuscript.

9. Long-term stability analysis

Type of analysis, bias conditions and environmental conditions
For instance: illumination type, temperature, atmosphere humidity, encapsulation method, preconditioning temperature

☒ Yes
☐ No

Stated in Method section.